

Automatic Imaging System With Decision Support for Inspection of Pigmented Skin Lesions and Melanoma Diagnosis

José Fernández Alcón, Călina Ciuhu, Warner ten Kate, Adrienne Heinrich, Natallia Uzunbajakava, Gertruud Krekels, Denny Siem, and Gerard de Haan

Abstract—In this paper, we describe an automatic system for inspection of pigmented skin lesions and melanoma diagnosis, which supports images of skin lesions acquired using a conventional (consumer level) digital camera. More importantly, our system includes a decision support component, which combines the outcome of the image classification with context knowledge such as skin type, age, gender, and affected body part. This allows the estimation of the personal risk of melanoma, so as to add confidence to the classification. We found that our system classified images with an accuracy of 86%, with a sensitivity of 94%, and specificity of 68%. The addition of context knowledge was indeed able to point to images that were erroneously classified as benign, albeit not to all of them.

Index Terms—Decision support, image classification, melanoma, skin lesions.

I. INTRODUCTION

MALIGNANT melanoma is the most aggressive and the deadliest form of skin cancer among the Caucasian population. The estimated number of new cases and deaths in the U.S. in 2008 is 62 480 and 8420, respectively [2]. Melanoma often has a slow early growth rate during which curable lesions may be detected and removed at a relatively low cost. This results in a high five-year survival rate of 95%. Progression of the disease in the late stage is associated with poor survival rate of 13% [9]. Due to the increase in incidence [16] and the consequent mortality, malignant melanoma represents a significant and growing public health problem. For instance, the total economical burden in the U.S. caused by melanoma can be estimated as 7 billion USD annually [4]. Therefore, earlier detection of melanoma is essential and still one of the most challenging problems in dermatology.

Despite the recently shown cost effectiveness of melanoma inspection, which was based on Markov model simulation [27],

there are no melanoma screening trials in the U.S. This is in contrast to the National Cancer Institute Prostate, Lung, Colorectal, and Ovarian Cancer Screening trial. Furthermore, no easy-to-access tool for melanoma screening exists, where the patients could get a consult without visiting an office of a general practitioner or a dermatologist.

To distinguish a benign lesion from a melanoma combined clinical and dermatoscopic criteria [12] are used such as in the ABCD(E)-formula: asymmetry, border irregularity, colour variation, a diameter >6 mm, and evolution. Other approaches would also be possible such as the ABCD rule of dermatoscopy [30] and the *seven-point checklist* [26]. Dermatoscopic examination, provided that the technique is used by well-trained and experienced physicians, is a valuable adjunct to clinical examination. Progress in early melanoma diagnosis was made when (digital) dermoscopy was introduced, and also computer algorithms have shown to contribute to a so-called automated melanoma diagnosis. For this, diagnoses features are identified that can be extracted from the digital image and which enable to distinguish between melanoma and benign lesions. The features are such that value ranges can be assigned within which the diagnosis can be made specific with high probability. The criteria of the ABCD(E)-formula are doing so to a certain extent. More objective criteria are of great importance to avoid a missed melanoma and on the other hand avoid unnecessary surgery of benign lesions. Such criteria include epidemiological ones (e.g., age, amount of lesions, sun burns) [11]. They are not specific in the sense that a diagnosis can be drawn from them alone. They indicate a general risk. Therefore, these criteria seem less effective to be used as features in the classification algorithms to distinguish between melanoma and benign lesions.

A number of companies and university groups are working on instruments and algorithms for automated melanoma diagnosis. All of them are based on image classification and a high resolution dedicated imaging system for data acquisition [18], [29], [38], [25], [40], [15], [41], [33], [32]. One of the early ones is the nevoscope [14].

In order to arrive at an automatic diagnosis system for improved early diagnosis, we took an approach in which the general (epidemiological) risk criteria are added to a classifier using the dermatoscopic ABCD feature set. The classifier remains to operate on the original feature set, and a Bayesian network is added to account for the additional criteria. In this way, we realized a decision support system tool that combines the outcome

Manuscript received April 15, 2008; revised October 15, 2008. Current version published February 19, 2009. The associate editor coordinating the review of this manuscript and approving it for publication was Dr. Rangaraj M. Rangayyan.

J. Fernández Alcón, C. Ciuhu, W. Kate, A. Heinrich, and N. Uzunbajakava are with Philips Research Laboratories, Eindhoven 5656AE, The Netherlands (e-mail: Calina.Ciuhu@philips.com).

G. Krekels and D. Siem are with Catharina Ziekenhuis, 5623 EJ Eindhoven, The Netherlands.

G. de Haan is with Eindhoven University of Technology, Eindhoven, The Netherlands.

Color versions of one or more of the figures in this paper are available online at <http://ieeexplore.ieee.org>.

Digital Object Identifier 10.1109/JSTSP.2008.2011156

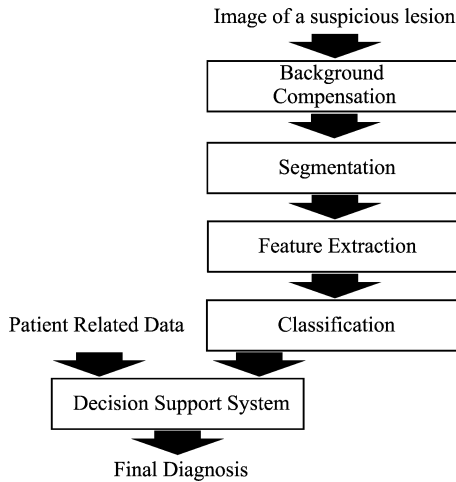


Fig. 1. Overall workflow of the automatic system for melanoma screening.

of image classification with the context knowledge about patient-related data such as skin type, age, gender, and affected body part.

In addition, the image classifier is designed for images of skin lesions acquired using a conventional, consumer-type of digital camera. Professional applications for skin imaging rely on high quality image acquisition devices, on professional help, and specific image acquisition protocols. The resulting picture quality is optimal for skin cancer detection purposes. However, our intention is to consider also non-professional, consumer applications, where a risk estimate rather than a diagnosis can be provided.

In this paper we describe the system. Its overall workflow is shown in Fig. 1. In Section II, we describe the image processing and the segmentation algorithm. In Section III we explain how we derive the features according to the dermatoscopic criteria. These features are used by a classifier, which is discussed in Section IV. The usage of context knowledge, which integrates the patient risk profile into the decision support system is explained in Section V. The results of validation are presented in Section VI. We finalize with conclusions in Section VII.

II. IMAGE PROCESSING AND SEGMENTATION ALGORITHM

As said, our intention is to consider non-professional applications, where the image classifier is designed for images acquired using a conventional, consumer-type of digital camera. Imaging skin is not an easy task, as it implies coping with skin irregularities and with a curved surface. Particularly for consumers, where imposing protocols is not the most appropriate solution, our experience is, that images will often be altered by uneven illumination. This artifact affects directly both the segmentation and the feature extraction algorithms.

In this section, we will first present a solution to compensate for uneven illumination. Furthermore we will elaborate on the lesion segmentation algorithm, which is necessary for the subsequent feature extraction and classification.

A. Segmentation

In Fig. 2, the image of a pigmented lesion which needs to be analyzed for diagnosis is displayed. To that end, we need to



Fig. 2. Typical input image.



Fig. 3. Erroneous segmentation results (red contour) caused by uneven background illumination.

separate the pigmented lesion from the background, for which we use segmentation algorithms. An overview of segmentation algorithms [35] suggests to use *edge detection*, *active contours and snakes*, or *clustering techniques—thresholding*.

Edge detection-based algorithms perform poorly when applied to skin images, mainly because of the presence of fine details and/or hair on the skin. *Snakes or active contours* [24] are less attractive because of the complex shape of the melanoma suspicious lesions. Since *thresholding* does not present any of these disadvantages and it has been used successfully in the past [41], we have selected it as the segmentation method.

As can be seen in Fig. 2, due to an incorrect positioning of the camera, and due to the fact that skin is usually not flat, the resulting image is not evenly illuminated. As a consequence, the distributions corresponding to the pigmented lesion and the shadowed background will overlap in the image histogram, forming the lower intensity peak, as seen in Fig. 4. The peak at higher intensity corresponds to the correctly illuminated background region.

Clearly, direct thresholding will result in erroneous segmentation, as illustrated in Fig. 3.

B. Background Correction

To prevent segmentation errors, we have to correct for the uneven illumination. To that end, we first realize that the uneven illumination corresponds to a low frequency spatial component of the image, while the information about the skin texture and the pigmented lesion are enclosed in the high spatial frequency component of the image. Therefore, we correct for uneven illumination by simply removing the low frequent spatial component of the image.

The effect of illumination correction on the image is shown in Fig. 6, the histogram of which is displayed in Fig. 5. Clearly, as compared to the histogram of the original image (Fig. 4), in the compensated image histogram (Fig. 5) the background is represented by a quasi-Gaussian distribution at higher intensity, while the lesion distribution at lower intensity slightly overlaps with the left tail of the background distribution.

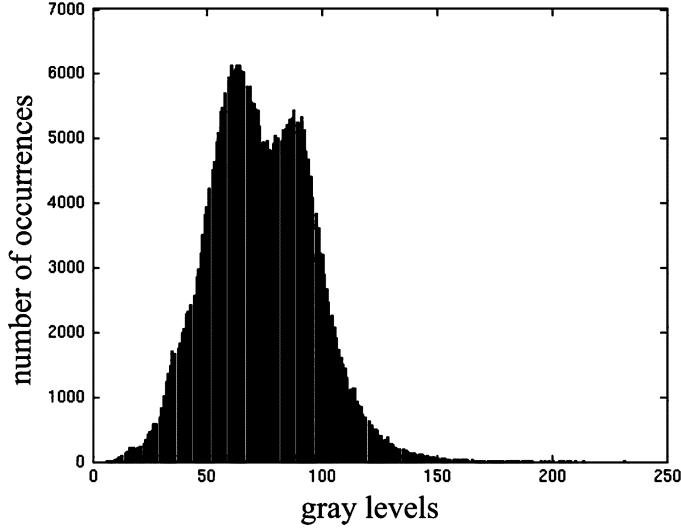


Fig. 4. Histogram of the original image.

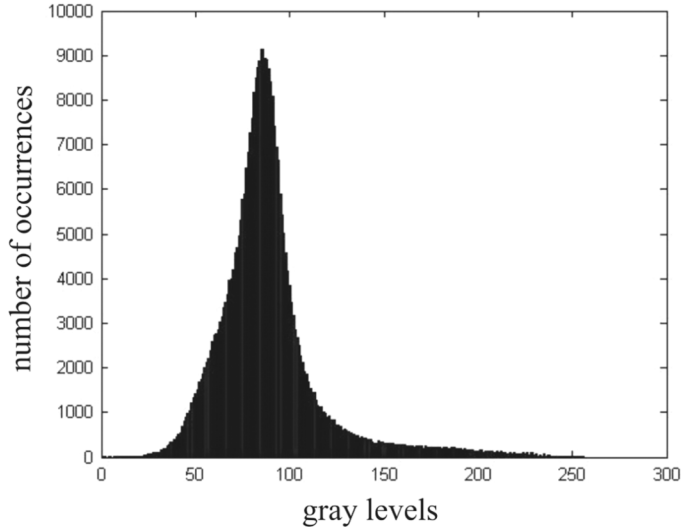


Fig. 5. Histogram of the background corrected image.



Fig. 6. Illumination-compensated image.

Furthermore, a clear improvement in the segmentation can be noticed in Fig. 7 when compared to Fig. 3. However, some signs of over-segmentation are present, when small adjacent regions of background are included in the segmented area of the pigmented lesion. This artifact may affect features related to the border quantification, therefore we will address them in the following section.



Fig. 7. Segmentation results (red contour) after background correction. Over-segmentation can also be noticed.

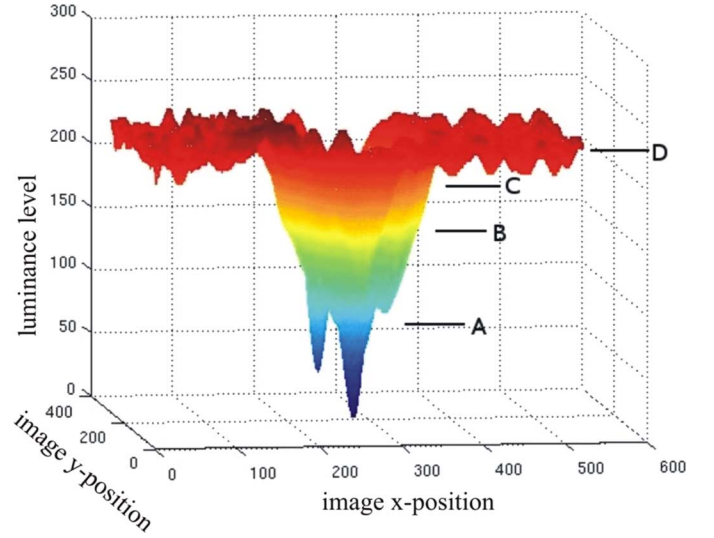


Fig. 8. Comparison between Otsu's algorithm threshold (C) and the proposed one (B).

C. Threshold-Based Segmentation

When implementing our thresholding method, we were inspired by Otsu's thresholding algorithm [31], which relies on maximizing the between-class variance.

Fig. 8 shows the 3-D representation of the luminance of a suspicious image. The blue-colored areas represent the pigmented lesion (areas with low luminance values), while the red colored ones represent the background (areas with high luminance values). Points A and D indicate the averages of the lesion distribution and background distribution, respectively.

Applying Otsu's algorithm we obtain a threshold which is very close to the centroid of the background distribution, as indicated by Point C in Fig. 8. This result is caused by the fact that the background distribution has a very low variance in comparison with the one of the suspicious lesion. As a consequence, over-segmentation may occur as illustrated in Fig. 7.

Ideally, the safest threshold is placed at half distance point between the average of the pigmented lesion (Point A) and the average of the background (Point D).

To implement this, we first realize that after the compensation for uneven illumination, the background is very smooth. Its histogram will correspond to a Gaussian-like distribution $f_b(x)$

$$f_b(x) = A \cdot e^{\frac{-(x-\mu_b)^2}{2\sigma^2}} \quad (1)$$

while the pigmented lesion distribution $f_p(x)$ remains unknown.

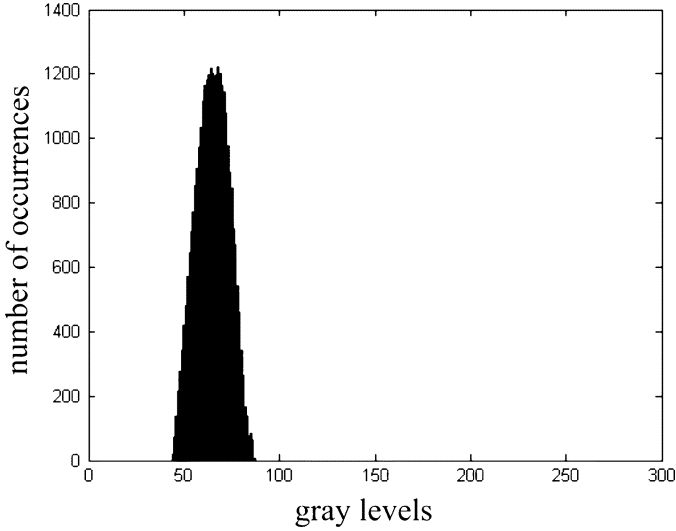


Fig. 9. Lesion distribution.

The probability distribution function of a background compensated image of a pigmented lesion will be the addition of the two distributions

$$f_{p+b}(x) = f_p(x) + f_b(x). \quad (2)$$

Assuming that the corresponding mean values are $\mu_p < \mu_b$, the right lobe of the background distribution $f_b(x)$ is less influenced by the lesion distribution $f_p(x)$ (see Fig. 5). The total distribution can be approximated as

$$f_{p+b}(x) = \begin{cases} f_b(x), & x \geq \mu_b \\ f_p(x) + f_b(x), & x < \mu_b. \end{cases} \quad (3)$$

In this model, we can reconstruct the background distribution by simply mirroring the right lobe with respect to the mean value μ_b , where μ_b is the peak in the histograms

$$\tilde{f}_b = \begin{cases} f_{p+b}(2\mu_b - x), & x < \mu_b \\ f_{p+b}(x), & x \geq \mu_b. \end{cases} \quad (4)$$

Finally, to obtain the lesion distribution, we simply subtract the Gaussian-like background distribution from the total histogram, as shown in Fig. 9

$$\tilde{f}_p(x) = f_{p+b}(x) - \tilde{f}_b(x). \quad (5)$$

We define the threshold selected by the proposed algorithm (Point B on Fig. 8), as the middle point T between the means $\tilde{E}(X_b)$ and $\tilde{E}(X_p)$ of the distributions $\tilde{f}_b(x)$ and $\tilde{f}_p(x)$, respectively

$$T = \frac{\tilde{E}(X_p) + \tilde{E}(X_b)}{2}. \quad (6)$$

This average is equally spaced from both centroids. Clearly, as compared to Fig. 7, in Fig. 10 the over-segmentation is eliminated.

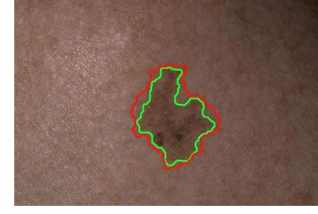


Fig. 10. Segmentation without over-segmentation (the green contour). The erroneous result is also displayed for comparison (the red contour).

TABLE I
SUMMARY OF THE SCORING OF THE ABCD RULE

Characteristic	Min. Score	Max. Score	Weight
Asymmetry	0	2	1.3
Border	0	8	0.1
Color	1	6	0.5
Differential Structures	1	5	0.5

III. FEATURE EXTRACTION

When the pigmented lesion is segmented, essential characteristics need to be extracted in order to decide whether the lesion is benign or malignant. In our implementation we followed the ABCD rule of dermatoscopy [30]. The ABCD rule is a semi-quantitative scoring rule where points are distributed according to the presence or severity of the four ABCD characteristics. The points are weighted and summed up to a total dermatoscopy score (TDS) where a higher risk of the lesion being malignant is indicated when a higher score is obtained. A description of the ABCD features is given in the following.

- **Asymmetry:** The lesion is bisected by two 90° axes. If asymmetric contours are observed with respect to both axes the score amounts to 2. If asymmetry is present with regard to only one axis, 1 point is given. If asymmetry is absent, a score of 0 is obtained.
- **Border:** The border of the lesion is divided into 8 regions, each of which is analyzed with regard to the sharpness or abruptness of the edge. For each region, in which the border is an abrupt cutoff of the pigment a point is given.
- **Color:** There are six different colors considered for the color score: white, red, light brown (lBrown), dark brown (dBrown), blue-gray (bGray), and black. For each color present in the lesion 1 point is added.
- **Differential Structures:** To obtain the differential structure score, five structural features are considered: network, homogeneous areas, dots, globules, and branched streaks. A point is given when one or more occurrences of the same structure are present.

Table I summarizes the scores and weights of the ABCD features. A TDS smaller than 4.75 indicates a benign lesion; a lesion is regarded as suspicious when a TDS between 4.8 and 5.45 is obtained. The values greater than 5.45 suggest a high melanoma risk.

In the design of the automatic feature extraction system the objective features are defined, in line with the subjective ABCD characteristics. Furthermore, modifications are carried out to

TABLE II
FEATURES EXTRACTED PER SAMPLE

Asymmetry features	$A_p, A_c, A_p/A_c$ (solidity), A_p/A_b (extent), $4A_p/\pi$ (equivalent diameter), $4\pi A_p/p_p^2$ (circularity), $p_p, b_p/a_p, b_b/a_b$, convex hull, eccentricity, entropy.
Border features	μ, σ^2
Color features	$\max(\mathbf{R}), \max(\mathbf{G}), \max(\mathbf{B}), \min(\mathbf{R}), \min(\mathbf{G}), \min(\mathbf{B}), \text{mean}(\mathbf{R}), \text{mean}(\mathbf{G}), \text{mean}(\mathbf{B}), \text{var}(\mathbf{R}), \text{var}(\mathbf{G}), \text{var}(\mathbf{B}), \text{mean}(\mathbf{R}), \text{mean}(\mathbf{G}), \text{mean}(\mathbf{B}), c_{\text{white}}, c_{\text{red}}, c_{\text{IBrown}}, c_{\text{dBrown}}, c_{\text{BGray}}, c_{\text{black}}$
Textural features	$\mathbf{E}^{[k]}, \mathbf{H}^{[k]}, \mathbf{C}_{\text{cor}}^{[k]}, \mathbf{C}_{\text{con}}^{[k]}, \text{mean}(\mathbf{E}^{[k]}), \text{mean}(\mathbf{H}^{[k]}), \text{mean}(\mathbf{C}_{\text{cor}}^{[k]}), \text{mean}(\mathbf{C}_{\text{con}}^{[k]})$

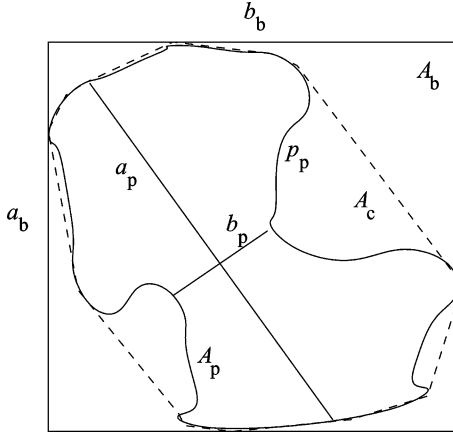


Fig. 11. Parameters of segmented pigmented area, convex hull (dashed) and bounding box.

comply with rotation and scale invariance. In the following, the automatic feature extraction is described and the features are summarized in Table II.

A. Quantification of the Asymmetry

Measuring the asymmetry and irregularity characteristics of a lesion is done with various features using the parameters given in Fig. 11, where A_p, A_c, A_b are the areas of the pigmented area, the convex hull and the bounding box, respectively. The axes of the pigmented area and the bounding box are given by a_p, b_p, a_b , and b_b and the perimeter of the lesion by p_p . All the computations regarding the border features are done on the binary image of the segmented lesion. Regarding the computations on the areas, the following parameters are used as features: $A_p, A_c, A_p/A_c$ (solidity), A_p/A_b (extent), $4A_p/\pi$ (equivalent diameter), $4\pi A_p/p_p^2$ (circularity). Furthermore, the perimeter p_p , the ratios b_p/a_p and b_b/a_b are calculated. Other features giving a more general description of the shape of the lesion, such as the convex hull, the eccentricity, measuring the similarity to a circle or ellipse, and the entropy [39], measuring the regularity of the border, are taken into account.

For scale invariance, the features, which are not inherently normalized, are divided by the longer lesion axis b_p .

B. Quantification of the Border

For reasons of rotation invariance, we restrained from dividing the border into eight portions and analyzing the sharp-

TABLE III
POSITIONING OF THE SIX POSSIBLE BASIC COLORS OF A PIGMENTED LESION ON THE RGB COLOR SPACE

Color	Red	Green	Blue
White	255	255	255
Red	204	51	51
Light Brown	153	102	0
Dark Brown	51	0	0
Blue Gray	51	153	255
Black	0	0	0

ness for each portion independently. Instead, local computations yielded one measure for the entire border.

The sharpness of the border is quantified by the magnitude of the gradient for each pixel of the border using *Sobel's* [36] Horizontal and Vertical Filters. However, due to slight inaccuracies in the segmentation of the pigmented area, the gradient computation on a dilated border produced a better separation between a benign and a malignant lesion. A satisfactory separation was experimentally found with a dilation of 2 pixels, producing a border of 5 pixels wide. With the above computation, two features are extracted, namely the average and the variance of the gradient magnitude for the entire border. They are given by

$$\mu = \frac{1}{N} \sum_{(x,y) \in \mathbf{B}} |\nabla I(x,y)|$$

$$\simeq \frac{1}{N} \sum_{(x,y) \in \mathbf{B}} |\nabla_r I(x,y)| \quad (7)$$

and

$$\sigma^2 = \frac{1}{N} \sum_{(x,y) \in \mathbf{B}} (|\nabla I(x,y)| - \mu)^2$$

$$\simeq \frac{1}{N} \sum_{(x,y) \in \mathbf{B}} (|\nabla_r I(x,y)| - \mu)^2 \quad (8)$$

where (x,y) denote the pixel coordinates of the set of border line pixels \mathbf{B} , I the grayscale values of the image, r the normal component of the border line, ∇_r the radial component of the gradient, and N the number of border line pixels.

C. Quantification of Color

Before computing the relevant color features, each RGB color channel of the segmented lesion is filtered with a Gaussian kernel to remove outliers, e.g., produced by noise.

The six basic colors of interest are defined with the RGB color space as given in Table III. For each pixel, the Euclidean distance to each of these six colors is computed and the counter of the nearest color, $c_{\text{white}}, c_{\text{red}}, c_{\text{IBrown}}, c_{\text{dBrown}}, c_{\text{BGray}},$ or c_{black} , is increased by $1/n$, with n the number of pixels within the segmented area.

In order to provide more color information to the classification algorithms described in the next section, also the RGB color channels themselves are analyzed more closely. The red, green, and blue components of each pixel are stored as an element in the respective $n \times 1$ vectors $\mathbf{R}, \mathbf{G},$ and \mathbf{B} . The features extracted from these vectors comprise a computation of the mean $\text{mean}(\cdot)$, the variance $\text{var}(\cdot)$, the maximum $\max(\cdot)$ and the minimum $\min(\cdot)$ of the vector components of $\mathbf{R}, \mathbf{G},$ and \mathbf{B} .

D. Quantification of Differential Structures

The differential structures mentioned in the ABCD rule are only visible in images which are acquired with a dermatoscope. With this device epiluminescence images are taken where sub-surface structures are magnified. As we do not intend to limit the design of the system to high quality images, the differential structure features as used in the ABCD rule are modified for this work. Other kind of texture information can be extracted which is available in images taken with a conventional digital camera. Therefore, texture characteristics are computed on the grayscale image components in the segmented area using the Haralick-features [22]. These are determined using gray-tone spatial-dependence matrices $D_s^{[k]}(i, j)$ ($k = 1, \dots, 4$) listing how many times the gray tones i and j are spatial neighbors. The matrix $D_s^{[k]}(i, j)$ is computed for each of the four angles $0^\circ, 45^\circ, 90^\circ, 135^\circ$, where k denotes the angle of spatial neighborhood. The four features *Energy*, *Homogeneity*, *Correlation* and *Contrast* were chosen based on their classification accuracy and computational cost. They are part of the most commonly used Haralick features [10] and are defined as

$$\mathbf{E}^{[k]} = \sum_{i,j} D_s^{[k]}(i, j)^2 \quad (9)$$

$$\mathbf{H}^{[k]} = \sum_{i,j} \frac{D_s^{[k]}(i, j)}{1 + |i - j|} \quad (10)$$

$$\mathbf{C}_{\text{cor}}^{[k]} = \sum_{i,j} \frac{(i - \mu_i)(j - \mu_j)D_s^{[k]}(i, j)}{\sigma_i \sigma_j} \quad (11)$$

$$\mathbf{C}_{\text{con}}^{[k]} = \sum_{i,j} |i - j|^2 D_s^{[k]}(i, j) \quad (12)$$

where μ_i, μ_j, σ_i and σ_j are the means and the standard deviations of the gray-tone spatial-dependence matrices $D_s^{[k]}$ with regard to the gray tones i and j . Furthermore, the means $\text{mean}(\mathbf{E}^{[k]})$, $\text{mean}(\mathbf{H}^{[k]})$, $\text{mean}(\mathbf{C}_{\text{cor}}^{[k]})$ and $\text{mean}(\mathbf{C}_{\text{con}}^{[k]})$ are added as separate features.

IV. CLASSIFICATION

The feature extraction step resulted in 55 features, which are potentially useful in discriminating a benign from a malignant lesion. Not all features are equally valuable for this classification task due to, e. g., redundancy or irrelevance. Additionally, it is difficult to experimentally analyze and explicitly recognize patterns in the data of a larger test set. Therefore, machine learning algorithms are usually applied to determine the most relevant features, as is done in e. g., [19], and to describe implicit patterns by employing attribute selection and classification algorithms.

In the course of this work, we pre-evaluated different combinations of attribute selection algorithms and classifiers. A comparison of attribute selection algorithms is given in [20] according to which a *correlation-based feature selector* (CFS) [21] is one of the most promising methods.

When the most reliable and relevant features f_1, \dots, f_n are selected, a classification function $c(f_1, f_2, \dots, f_n)$ computes the decision $d \in \{\text{Melanoma}, \text{Nevus}\}$. The following classifiers were selected: A decision tree learner (J48), a computationally cheaper decision tree with only a single depth (Deci-

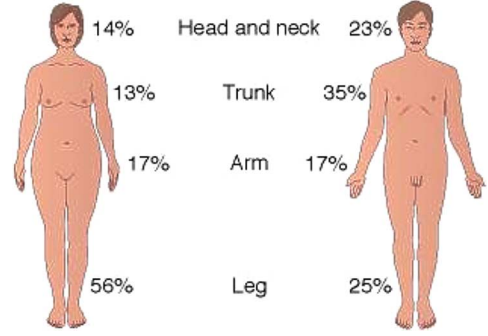


Fig. 12. Melanoma incidence by part of the body and gender [5].

sion Stump), a more sophisticated tree with linear logistic regression models at the leaves (Logistic Model Trees (LMT)), a probabilistic learning method (Bayesian Networks) and the meta-classifier AdaBoost which takes the mentioned classifiers as subordinate algorithms and uses them as variables and replaceable parameters.

V. CONTEXT KNOWLEDGE: PATIENT RISK GROUP

Dermatologists do not base their diagnosis solely on the analysis of the skin lesion. Patient-related context is also of relevance in making a diagnosis. *The same lesion could be diagnosed as highly dangerous if it is on the leg of an Irish female and benign if the bearer is an Italian male.* This relates to the inherent overlap in feature distribution of malignant and benign lesions, as for example depicted by Fig. 16. The dermatologist distinguishes different populations characterized by factors like age, gender, sun-burn history, hair color, number of nevi, and personal disease history as well as melanoma occurrence in the family [13]. The risk population the patient belongs to is taken into account in the diagnosis. In our prototype we did not consider all of the available risk factors, but we selected four major ones. These were the following.

Skin Type. The Fitzpatrick skin type classification distinguishes six different skin phototypes named from I to VI. Skin types I always burns and never tans, while a skin type III–IV rarely burns and tans with ease. The skin types V and VI are dark skins. The melanoma risk of a person with skin type I is ten times greater than of one with skin type VI [6]. The melanoma incidence distributed over the skin types is shown in Table IV.

Age: Age is a relevant factor for melanoma diagnosis. The older the person is the higher the risk [8]. See Table V.

Gender: Melanoma incidence is higher in males than in females [1].

Part of the Body: Melanomas have different incidence rates depending on the part of the body and the gender, see Fig. 12 [5].

We built a decision support system (DSS) that combines both sources of information: the classification of the image on the one hand and the patient population's likelihood of being affected on the other hand (see Fig. 1). The classifier is based on pattern recognition, and trained by given samples, as described in the previous sections. The context knowledge is modeled through a Bayesian Network (BN).

TABLE IV
MELANOMA DISTRIBUTION OVER SKIN TYPES

Skin Type	Melanoma Distribution
Skin Type I	35%
Skin Type II	39%
Skin Type III	16%
Skin Type IV	7%
Skin Type V	3.5%
Skin Type VI	3.5%

TABLE V
AGE DEPENDENT MELANOMA INCIDENCE [8]

Age	Number of melanomas
<10 years	Very rare
10 to 19 years	1%
20 to 39 years	13%
40 to 59 years	35%
> 60	51.0%

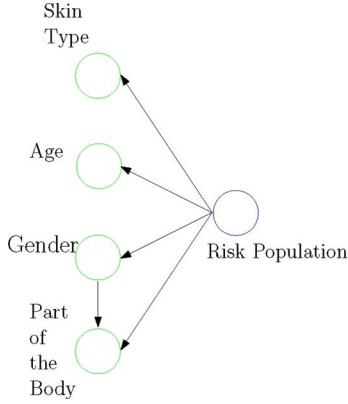


Fig. 13. BN modeling context knowledge.

Fig. 13 depicts such a BN that models the four factors: skin, age, gender, and body part. The node “Risk Population” (*RGrp*) has the states M and N , for being in a melanoma or nevus group, respectively. The prior probability of being in the melanoma group is set to its occurrence frequency over the world population, or, when the tool is used in a hospital, over the population presenting themselves for examination. The likelihoods $P(F|M)$ of being in the melanoma group for each of the four modeled factors F , are given as indicated above [1], [5], [6], [8]. The likelihoods $P(F|N)$ of not being in the melanoma group (but in the nevus group) with the corresponding factors are taken from the distributions of these factors over the world population (respectively, hospital visitors). Since we did not have access to all these numbers, we assumed a uniform distribution.

When knowing a factor’s value one can introduce it in the BN as evidence E , i.e., $F = E$, such that the BN can compute the (posterior) probability $P(M|E)$ of being in the melanoma group. Based on Bayes’ rule, the posterior probability can be computed as

$$P(M|E) = \frac{P(F|M) \cdot P(M)}{P(E)}. \quad (13)$$

Since $P(M)$ is a small value, the posterior probability of being in the risk group is low. Therefore, it is more useful to observe the change in this probability. This can be done through

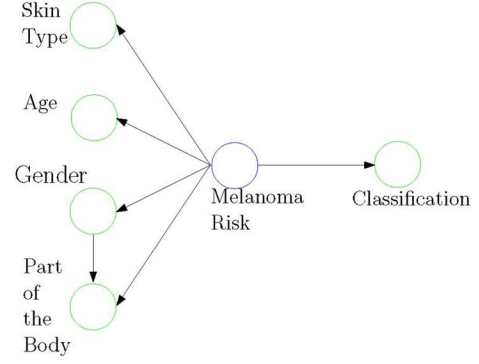


Fig. 14. BN modeling classifier with context knowledge.

observing the odds ratio between posterior and prior odds. The odds $O(H)$ is the ratio between the probability $P(H)$ on the event H occurring and the probability $P(\neg H)$ on the event not occurring [34]

$$\begin{aligned} O(M|E) &= \frac{P(M|E)}{P(\neg M|E)} = \frac{P(F|M) \cdot P(M)}{P(F|\neg M) \cdot P(\neg M)} \\ &= L(F|M) \cdot O(M) \end{aligned} \quad (14)$$

where $L(F|M)$ is the likelihood ratio, which can be seen to equal the odds ratio

$$L(F|M) = \frac{O(M|E)}{O(M)} = \frac{P(F|M)}{P(F|\neg M)}. \quad (15)$$

So, by observing the prior and posterior probability of being in the melanoma risk group, the odds increase (ratio) can be computed for a complex of evidence factors through the BN. As (15) shows, this increase is independent of the choice of the prior probability. (In general, each subsequently entered evidence updates the odds by the likelihood ratio corresponding to that evidence [34]). By setting the prior probability $P(M) = P(N) = 0.5$ the prior odds equals unity, and only the posterior odds needs to be observed. Such a choice also prevents that the BN has to calculate with probability values that are close to zero and one. In principle, the odds ratio ranges from 0 to ∞ . A value larger (less) than 1 means the patient is at more (less) risk than a randomly selected person. By using an appropriate function this range can be mapped to the $[0, 1]$ range.

The purpose of the DSS is to assist in setting an accurate diagnosis. To that end, the classifier and the BN were integrated in a unified BN. In our simplified prototype to demonstrate the approach this was achieved by extending the BN with an additional node that represents the classifier’s outcome, as shown in Fig. 14. In this model, the node “Classification” has two states, Malignant (M) and Benign (B). Note the difference with the node “Melanoma Risk” (which was labeled “Risk Population” in Fig. 13). The former models the classifier outcome, the latter models the probability of being diagnosed with melanoma, accounting for both the classifier outcome and the context factors. The outcome of the classifier is submitted to the BN as evidence to the node “Classification”. As far as the patient specific data are available, they are entered as evidence to the corresponding nodes. Otherwise, they are left “unknown”.

The dependence relation between the two nodes, i.e., the conditional probabilities of the states at “Classification” (Class) given the state at “Melanoma Risk” (*RGrp*), is modeled according to the measured true positive (TP) and true negative (TN) rates of the classifier, i.e., the percentage correct when provided with an image that is a melanoma or nevi, respectively

$$\begin{aligned} P(\text{Class} = M \mid RGrp = M) &= \text{TP} = 0.9 \\ P(\text{Class} = B \mid RGrp = M) &= \text{FN} = 0.1 \\ P(\text{Class} = M \mid RGrp = N) &= \text{FP} = 0.3 \\ P(\text{Class} = B \mid RGrp = N) &= \text{TN} = 0.7. \end{aligned} \quad (16)$$

As said, the schema in Fig. 14 is a simplified form. It does integrate the two sources of observations, image classification and risk group estimation, however, its estimate is that of an average probability. The dependency link between the Melanoma Risk and Classification node captures the conditional probability in average, as given by the TP and TN rates of the classifier. A further measure would be to include the confidence in the classifier’s decision. In its most simple form, the classifier’s decision is expressed as, see also (19)

$$\forall i : \mathbf{w}_i^T \cdot \mathbf{x} > c_i \quad (17)$$

where \mathbf{x} represents the feature set, \mathbf{w}_i the weights on them, and c_i the threshold. Different decision planes can be defined, indicated by the index i . This classification scheme can be refined in many ways, see, for example [17].

One approach to include the confidence in the classification is to estimate the probability distributions for M and B classification over the feature set, and use their ratio at a given observation to estimate the confidence. Another approach is to observe the distance of the observed feature set to the decision planes, $|\mathbf{w}^T \cdot \mathbf{x} - c|$. In our prototype, we displayed this distance in the user interface. Next to the distance to the decision plane, the confidence level depends on the variance in the probability distribution (in feature space). This variance could be estimated from the training samples in the usual way. Then, the conditional probabilities connecting the Melanoma Risk node with the Classification node, see (16), could be modified as follows, for example

$$\begin{aligned} P(\text{Class} = M \mid RGrp = M) &= 1 - (\beta_0 - \text{TP}) \exp^{-\frac{1}{2} \left(\frac{\mathbf{w}_M^T \cdot \mathbf{x} - c}{t \cdot \sigma_M} \right)^2} \\ P(\text{Class} = B \mid RGrp = N) &= 1 - (\beta_1 - \text{TN}) \exp^{-\frac{1}{2} \left(\frac{\mathbf{w}_B^T \cdot \mathbf{x} - c}{t \cdot \sigma_B} \right)^2} \end{aligned} \quad (18)$$

where σ_M^2 and σ_B^2 are the estimated variance in the training data with malignant and benign samples, respectively, and t is a scaling factor to assign the confidence interval. β_0 and β_1 provide further models of the classifier’s confidence. At full accuracy they equal 1. Although artificial, this definition has the effect that observed feature sets in the neighborhood of the threshold receive the classifier’s TP (respectively, TN) probability, while when they are distant receive full confidence of a correct classification. (A further refinement would be

to account for being at the critical or noncritical side of the threshold in terms of the diagnostic outcome.) In this way, the node “Melanoma Risk” holds the risk based on both the prior risk known from the membership in a population subgroup, the classification of the image, and the confidence in that classification. There is still a discontinuity due to the binary decision of the classifier of which the BN assumes the classifier is correct, and takes the decision as evidence. Around the threshold the BN should rather treat the state of the classifier node as unknown. This can be solved by computing the odds for both classification outcomes and weighing them according to confidence in the classifier.

VI. RESULTS AND DISCUSSION

The system was tested in two stages. In the first stage we evaluated the classifier in classifying images of pigmented lesions, in the second stage we investigated the integral system, when the context knowledge is added to the classifier’s outcome. The quality of the classifier was assessed using the common measures of sensitivity and specificity. We evaluated the contribution of the additional context knowledge to the decision support system by interviewing experts.

A. Attribute Selection and Classifier Algorithms

In order to evaluate the chosen attribute selection and classifier algorithms, we carried out experiments on a data set comprising 152 images taken from the *Dermnet* dataset [3]: 45 *Clark Nevi* (benign) and 107 *Malignant Melanoma* (malignant). Each image was background-compensated and segmented before extracting a total of 55 features as described in Section III. For the initial benchmarking, we used Weka (Waikato Environment for Knowledge Analysis) [7], an open-source Java-based machine learning tool. We have applied 10-fold cross-validation.

The classification accuracies of the tested classifiers combined with the attribute selection algorithm CFS are shown in Table VI. Since the data set is relatively small, the two best combinations CFS + LMT and CFS + AdaBoost + LMT can be considered as performing equally well. Both of them also give the highest areas under the respective ROC curves: 0.89 for CFS + LMT, see Fig. 15, and 0.91 for CFS + AdaBoost + LMT. However, the combination of CFS + LMT requires only a simple implementation with much lower computational complexity than AdaBoost. With the CFS + LMT algorithm a classification accuracy of 86% and a sensitivity of 94%, (see Table VIII) is achieved. The specificity amounts to 68%. LMT is a decision tree whose leaves are a linear combination of the features in the form of

$$c(f_1, \dots, f_n) = \begin{cases} \text{Nevus}, & \text{if } \sum_{i=1}^n w_i f_i \geq d_{\text{thres}} \\ \text{Melanoma}, & \text{if } \sum_{i=1}^n w_i f_i < d_{\text{thres}} \end{cases} \quad (19)$$

where w_1, \dots, w_n are the corresponding weights and d_{thres} the threshold for the decision variable. For the small number of features obtained (see Table VII), the resulting tree has only one leaf, thus behaving as a simple linear function. The distribution of the nevi and melanomas is shown in Fig. 16 where a Gaussian is fitted on the output of the linear combination. Second, the confusion matrices depicted in Tables VIII and IX show a higher

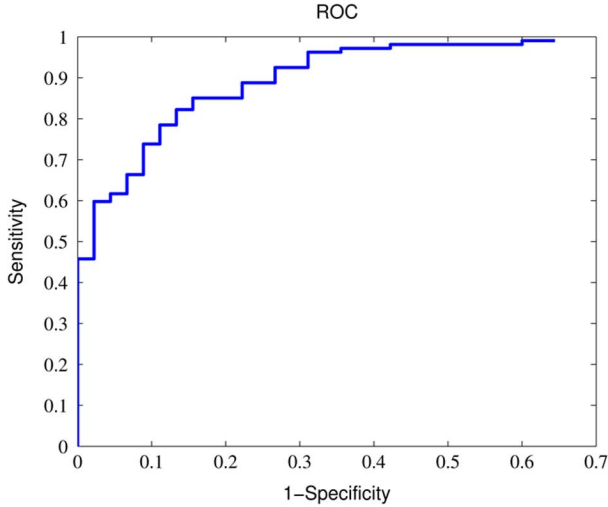
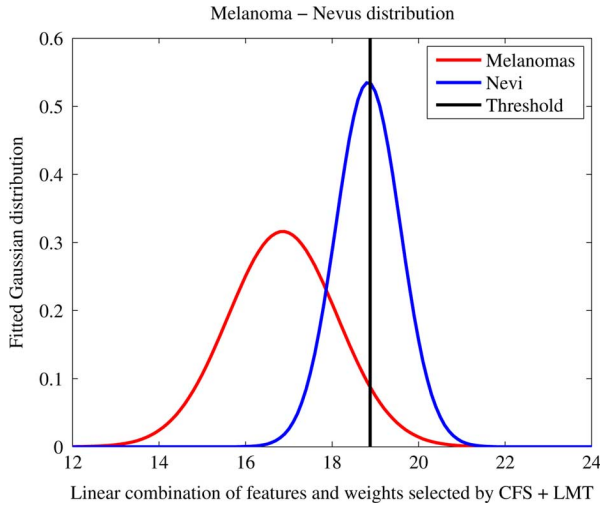


Fig. 15. ROC curve for the LMT classifier using CFS.

Fig. 16. Fitted Gaussian distribution of melanomas and nevi on $\sum_{i=1}^n w_i f_i$. The linear combination and threshold are given by the LMT classifier using CFS.TABLE VI
CLASSIFICATION ACCURACIES OF ATTRIBUTE SELECTION
AND CLASSIFICATION ALGORITHMS

Meta Classifier	Algorithm	No Attr. Selection	CFS
	Decision Stump	67.8%	67.7%
	J48	78.3%	80.9%
	LMT	82.9%	86.8%
	Bayesian Network	78.9%	80.3%
AdaBoost	Decision Stump	76.3%	80.9%
AdaBoost	J48	80.3 %	83.5%
AdaBoost	LMT	85.5%	85.5%
AdaBoost	Bayesian Network	82.2%	79.6%

sensitivity for LMT than for AdaBoost (94% versus 89%, respectively), which is rather important in this context since it is desired to reduce the number of false negatives as much as possible.

TABLE VII
SELECTED FEATURES AND THEIR WEIGHTS FOR THE
LMT CLASSIFIER USING CFS

Feature	Weight
solidity	17
min(R)	0.01
mean(G)	2.79
mean(B)	-0.01
μ	-0.01
$C_{con}^{[1]}$	-8.16

TABLE VIII
CFS + LMT CONFUSION MATRIX

	Classified as Nevus	Classified as Mel.
Nevus	31	14
Mel.	6	101

TABLE IX
CFS + AdaBoost + LMT CONFUSION MATRIX

	Classified as Nevus	Classified as Mel.
Nevus	34	11
Mel.	11	96

B. Context Knowledge and Decision Support

To analyze how our integral approach performs, we examined a few cases of which the appearance-based diagnosis was difficult. Eventual histological inspection revealed that except for a few, most of them were malignant. When offered to our system, all cases were classified as benign lesions, i.e., they were to the right of the threshold in Fig. 16. The output of our prototype system yields three quantities. The first is the classification *decision* obtained by comparing the melanoma probability with the trained threshold. Second, a *confidence measure* is given, associated to this decision. It depends on the numerical distance between the weighed feature sum and the threshold. Third, the *odds increase* is reported, which indicates how the objective criteria influence the likelihood on melanoma. All this information is interpreted together in the following manner: Given the decision is benign,

- if the confidence measure is small and the odds increase: definitely reconsider the benign decision;
- if the confidence measure is small and the odds decrease: reconsider the benign decision;
- if the confidence measure is large and the odds increase: still trust the benign decision;
- if the confidence measure is large and the odds decrease: trust the benign decision.

A similar reasoning holds for the malignant decision.

Figs. 17–20 indicate the results for four cases. The ground truth resulting after the histology analysis diagnosed all four malignant. Clearly, the classifier had difficulties in classifying correctly, as the confidence measure confirms.

Fig. 17 indicates a low confidence measure (as compared to the standard deviation of the class distributions, estimated to about 1.3). Hence, one should definitely reconsider the case (do not trust the benign decision). Yet a similar case is represented in Fig. 18, in which the confidence measure is relatively small, but the odds increase is very large. Fig. 19 also has relatively

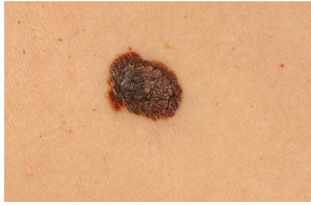


Fig. 17. Lesion example 1. Context knowledge: skin type II, mature, female, torso. Confidence measure is 0.13. Odds increase is 1.13.



Fig. 18. Lesion example 2. Context knowledge: skin type I, senior, male, arm. Confidence measure is 1.17. Odds increase is 4.41.



Fig. 19. Lesion example 3. Context knowledge: skin type I, mature, female, torso. Confidence measure is 1.46. Odds increase is 0.90.



Fig. 20. Lesion example 4. Context knowledge: skin type I, senior, male, torso. Confidence measure is 2.91. Odds increase is 5.18.

small confidence measure, but the odds decrease. According to the above rules, that would result in reconsideration of the case, although not in a strong way. The most doubtful result is indicated in Fig. 20. In this case, the system does not help to derive the proper diagnosis.

These results show that the context knowledge can be helpful in diagnosing lesions. We present here a first approach. The results are promising, but at the same time indicate that further improvement are possible. This can be along several ways. The precise way of accounting for context knowledge can be refined. Whether the classification accuracy can be improved by incorporating context knowledge as feature in the classifier needs more investigation. The confidence measure we have used is arbitrarily chosen and therefore might not be optimal. A similar argument applies to the rules to interpret the *decision*, *confidence measure*, and the *odds increase* results. The Bayesian network needs to be extended with other types of context knowledge. The probabilities it is loaded with were a first estimate. This can be

improved by taking into account the reports of more extensive epidemiological studies. More cases need to be studied followed by clinical validation to qualify the potential of this approach.

VII. CONCLUSION

In this paper, we described an automatic system for inspection of pigmented skin lesions and discriminating between malignant and benign lesions. The system includes a dedicated image processing system for feature extraction and classification, and patient-related data decision support machinery for calculating a personal risk factor.

It has been shown that our algorithm is capable of recreating controlled lighting conditions and correcting for uneven illumination. A robust segmentation algorithm has been developed. As a result, the features used for classification are scale and rotation invariant. Therefore, the distance at which the digital image was taken is of no significant importance as long as the size of the feature of interest can be resolved on an imaging device. This allows image acquisition using a conventional digital camera.

The accuracy of our classifier was 86% with 94% sensitivity and 68% specificity. This is comparable with the results shown in literature [23], [32] and [28] and is comparable to the accuracy of detection shown by general practitioner and study dermatologists [37].

Furthermore, the results have shown that including the patient related data is beneficial for the diagnosis.

The proposed system is a first proof-of-concept model of which the efficiency, sensitivity and specificity can be improved in future research. Additionally, the outcome of the histopathology, which is still regarded as the Gold Standard in the diagnosis of malignant melanoma, can be fed back to the here presented automatic diagnosis system. By the means of such a feedback system, the performance of the proposed system can be inherently improved.

We anticipate that the proposed system can serve as a basis for an easy-to-access melanoma screening service, where the range of potential users includes dermatologists, general practitioners, as well as laymen not specifically trained in the field. The system provides an ample opportunity for teledermatology, where the application range can be extended to different forms of skin cancer as well as other skin conditions.

REFERENCES

- [1] *2007 Skin Cancer Facts*, [Online]. Available: <http://www.skincancer.org/skincancer-facts.php>, Skin Cancer Foundation, Tech. Rep.
- [2] *Cancer Facts and Figures 2008*, [Online]. Available: <http://www.cancer.org/downloads/STT/2008CAFFfinalsecured.pdf>, Tech. Rep.
- [3] *Dermnet Skin Disease Image Atlas*, [Online]. Available: www.dermnet.com
- [4] *Melanoma Project*, [Online]. Available: <http://www.bionorth.org.il/BioNorth/SendFile.asp?GID=446>
- [5] *Melanoma Symptoms*, [Online]. Available: <http://www.cancerhelp.org/help/default.asp?page=3009>, National Institute for Health and Clinical Excellence, Tech. Rep.
- [6] *Skin Cancer: Basal Cell Carcinoma, Squamous Cell Carcinoma, and Malignant Melanoma*, [Online]. Available: <http://www.clevelandclinic.org/health/health-info/docs/1800/1852.asp?index=8090>, Cleveland Clinic Center for Consumer Health Information, Tech. Rep.
- [7] *Weka*, [Online]. Available: <http://www.cs.waikato.ac.nz/ml/weka/>
- [8] *Who is at Risk of Melanoma*, [Online]. Available: <http://www.dermnetnz.org/lesions/melanoma.html>, New Zealand Dermatological Society Incorporated, Tech. Rep.

- [9] U.S. Emerging Melanoma Therapeutics Market, a090-52, Tech. Rep., 2001.
- [10] J. J. Aucouturier, M. Aurnhammer, and F. Pachet, "Second-order statistics are less important for audio textures than for image textures," 2008 [Online]. Available: <http://citeseerx.ist.psu.edu/viewdoc/summary?doi=10.1.1.74.291>
- [11] J. P. Banky, J. W. Kelly, D. R. English, J. M. Yeatman, and J. P. Dowling, "Incidence of new and changed nevi and melanomas detected using baseline images and dermoscopy in patients at high risk for melanoma," *Arch. Dermatol.*, vol. 141, no. 8, pp. 998–1006, Aug. 2005.
- [12] A. Blum, G. Rassner, and C. Garbe, "Modified abc-point list of dermoscopy: A simplified and highly accurate dermoscopic algorithm for the diagnosis of cutaneous melanocytic lesions," *J. Am Acad. Dermatol.*, vol. 48, no. 5, pp. 672–678, May 2003.
- [13] E. Cho, B. Rosner, D. Feskanich, and G. Colditz, "Risk factors and individual probabilities of melanoma for whites," *J. Clin. Oncol.*, vol. 23, no. 12, pp. 2669–2675, 2005.
- [14] A. P. Dhawan, "An expert system for the early detection of melanoma using knowledge-based image analysis," *Anal. Quant. Cytol. Histol.*, vol. 10, no. 6, pp. 405–16, Dec. 1988.
- [15] A. P. Dhawan and A. Sicsu, "Segmentation of images of skin lesions using color and texture information of surface pigmentation," *Comput. Med. Imag. Graph.*, vol. 16, no. 3, pp. 163–177, 1992.
- [16] T. L. Diepgen and V. Mahler, "The epidemiology of skin cancer," *Brit. J. Dermatol.*, vol. 146, pp. 1–6, Apr. 2002.
- [17] R. O. Duda, P. E. Hart, and D. G. Stork, *Pattern Classification*. New York: Wiley Interscience, 2001.
- [18] M. Elbaum, "Computer-aided melanoma diagnosis," *Dermatol. Clinics*, vol. 20, no. 4, pp. 735–747, Oct. 2002.
- [19] H. Ganster, A. Pinz, R. Rhrer, E. Wildling, M. Binder, and H. Ki, "Automated melanoma recognition," *IEEE Trans. Med. Imag.*, vol. 20, no. 3, pp. 233–239, Mar. 2001.
- [20] M. A. Hall and G. Holmes, "Benchmarking attribute selection techniques for discrete class data mining," *IEEE Trans. Knowl. Data Eng.*, vol. 15, no. 6, pp. 1437–1447, Nov.–Dec. 2003.
- [21] M. A. Hall, "Correlation-based feature selection for discrete and numeric class machine learning," in *Proc. 17th Int. Conf. Machine Learning*, Jun. 2000, pp. 359–366, Morgan Kaufmann.
- [22] R. M. Haralick, K. Shanmugam, and I. Dinstein, "Textural features for image classification," *IEEE Trans. Syst., Man, Cybern.*, vol. 3, no. 6, pp. 610–621, Nov. 1973.
- [23] H. Lyatomi, H. Oka, M. Hashimoto, M. Tanaka, and K. Ogawa, "An internet-based melanoma diagnostic system—Toward the practical application," in *Proc. 2005 IEEE Symp. Computational Intelligence in Bioinformatics and Computational Biology*, Nov. 2005, pp. 1–4.
- [24] M. Kass, A. Witkin, and D. Terzopoulos, "Snakes: Active contour models," *Int. J. Comput. Vis.*, vol. 1, no. 4, pp. 321–331, 1988.
- [25] T. K. Lee, M. S. Atkins, R. P. Gallagher, C. E. MacAulay, A. Goldman, and D. I. McLean, "Describing the structural shape of melanocytic lesions," in *Proc. SPIE, Medical Imaging 1999: Image Processing*, 1999, vol. 3661, pp. 1170–1179.
- [26] W. Liu, D. Hill, A. Gibbs, M. Tempany, C. Howe, R. Borland, M. Morand, and J. Kelly, "What features do patients notice that help to distinguish between benign pigmented lesions and melanomas?: The ABCD(E) rule versus the seven-point checklist," *Melanoma Res.*, vol. 15, no. 6, pp. 549–554, 2005.
- [27] E. Losina, R. P. Walensky, A. Geller, F. C. Beddingfield, L. Wolf, B. A. Gilchrist, and K. A. Freedberg, "Visual screening for malignant melanoma, a cost-effectiveness analysis," *Arch. Dermatol.*, vol. 143, pp. 21–28, 2007.
- [28] S. Merler, C. Furlanello, B. Larcher, and A. Sboner, "Tuning cost-sensitive boosting and its application to melanoma diagnosis," in *Proc. 2nd Int. Workshop on Multiple Classifier System*, 2001, vol. 2096, pp. 32–42, ser. Lecture Notes In Computer Science.
- [29] M. Moncrieff, S. Cotton, E. Claridge, and P. Hall, "Spectrophotometric intracutaneous analysis—A new technique for imaging pigmented skin lesions," *Brit. J. Dermatol.*, vol. 146, no. 3, pp. 448–457, 2002.
- [30] F. Nachbar, W. Stolz, T. Merkle, A. B. Cognetta, T. Vogt, M. Landthaler, P. Bilek, O. Braun-Falco, and G. Plewig, "The ABCD rule of dermatoscopy: High prospective value in the diagnosis of doubtful melanocytic skin lesions," *J. Amer. Acad. Dermatol.*, vol. 30, no. 4, pp. 551–559, Apr. 1994.
- [31] N. Otsu, "A threshold selection method from gray-level histograms," *IEEE Trans. Syst., Man, Cybern.*, vol. 9, no. 1, pp. 62–66, Jan. 1979.
- [32] S. V. Patwardhan, S. Dai, and A. P. Dhawan, "Multi-spectral image analysis and classification of melanoma using fuzzy membership based partitions," *Computeriz. Med. Imag. Graph.*, vol. 29, pp. 287–296, 2005.
- [33] S. V. Patwardhan, A. P. Dhawan, and P. A. Relue, "Classification of melanoma using tree structured wavelet transforms," *Comput. Methods and Progr. in Biomed.*, vol. 72, 2003.
- [34] J. Pearl, *Probabilistic Reasoning in Intelligent Systems*. San Mateo, CA: Morgan Kaufmann, 1988.
- [35] *Color Image Segmentation: A State-of-the-Art Survey*. New Delhi, India: Proc. Indian Nat. Science Academy, Mar. 2001, vol. 67 A, Arch Dermatol.
- [36] I. Sobel and G. Feldman, "A 3×3 isotropic gradient operator for image processing," presented at the Stanford Artificial Project, 1968, unpublished.
- [37] W. Stolz, O. Braun-Falco, P. Bilek, M. Landthaler, W. Burgdorf, A. Cognetta, and B. Armand, *Color Atlas of Dermoscopy—2nd Enlarged and Completely Revised Edition*. Oxford, U.K.: Blackwell, 2002.
- [38] H. Talbot and L. Bischof, "An overview of the polartechnics solarscan melanoma diagnosis algorithms," in *Proc. APRS Workshop on Digital Image Computing*, 2003, pp. 33–38.
- [39] A. M. Tekalp, *Digital Video Processing*. Englewood Cliffs, NJ: Prentice-Hall, 1995.
- [40] S. Tomatis, M. Carrara, A. Bono, C. Bartoli, M. Lualdi, G. Tragni, A. Colombo, and R. Marchesini, "Automated melanoma detection with a novel multispectral imaging system: Results of a prospective study," *Phys. Med. Biol.*, vol. 50, pp. 1675–1687, 2005.
- [41] L. Xu, M. Jackowski, A. Goshtasby, D. Roseman, S. Bines, C. Yu, A. P. Dhawan, and A. Huntley, "Segmentation of skin cancer images," *Image Vis. Comput.*, vol. 17, pp. 65–74, 1999.



Jose Fernandez-Alcon was born in St. Louis, MO, in 1982. He studied electrical engineering at the Universidad Politecnica de Madrid, Madrid, Spain, and at Technische Universiteit Eindhoven, Eindhoven, The Netherlands. He received the M.Sc. degree in 2007 from the Technische Universiteit Eindhoven.

After a trainee period at the European Space Agency, he joined Dutch Space, Leiden, The Netherlands, working on the fields of simulation and grid computing.



Calina Ciuhu was born in Corabia, Romania, in 1974. She graduated in theoretical physics from the Babes-Bolyai University, Cluj-Napoca, and received the Ph.D. degree from Vrije Universiteit Amsterdam, Amsterdam, The Netherlands, in 2003.

In the same year, she became a Senior Scientist in the Video Processing and Analysis group of the Philips Research Laboratories, Eindhoven, The Netherlands. Her expertise varies from video processing for TV to image analysis for biomedical data.



Warner ten Kate studied electrical engineering at Delft University of Technology, Delft, The Netherlands, where he received the Ph.D. degree in 1987. His graduation work concerned silicon sensors.

He joined Philips Research Laboratories, Eindhoven, The Netherlands, where he developed compression algorithms for multichannel audio signals. This work has contributed to the MPEG2 standard. After doing research on internet multimedia applications, in particular on hypermedia presentation and audio streaming, his interest moved to reasoning algorithms for decision support systems. Part of this work contributed to the W3C SMIL recommendation. His current interest has returned into signal processing of biomechanical sensor signals and its combination with reasoning for realizing monitoring applications in wellbeing. The results of this research have been published in conference and journal papers. Some ideas have been patented or are patent applications.



Adrienne Heinrich was born in Zurich, Switzerland, in 1980. She studied electrical engineering and information technology at the ETH Zurich, where she received the M.Sc. degree in 2006.

In the same year, she joined the Video Processing and Analysis Group of Philips Research Laboratories, Eindhoven, The Netherlands. Currently, she is a Research Scientist, working to improve algorithms in the area of motion estimation and picture rate conversion.



Denny Siem received the M.D. degree from Erasmus Medisch Centrum, Rotterdam, The Netherlands, in 2007.

Since 2007, he has been with the Dermatology Department of the Catharina Hospital Eindhoven, Eindhoven, The Netherlands. He is pursuing a position as a Dermatologist in Training.



Natallia Uzunbajakava received the M.S. and Ph.D. degrees in applied physics from the University of Twente, Enschede, The Netherlands.

In 2004, she joined the Department of Biomedical Photonics, and later moved to the Department Care and Health Applications at Philips Research Laboratories, Eindhoven, The Netherlands. Currently, in her role as Senior Scientist, she focuses on application-oriented research in the fields of biophysics, tissue optics, and non-invasive diagnostics.



Gertruud Krekels received the M.D. degree in 1993 and the Ph.D. degree in 1998 for research on Basal cell carcinoma, both from the University of Amsterdam, Amsterdam, The Netherlands.

She is a Dermatologist with Catharina Hospital Eindhoven, Eindhoven, The Netherlands. She has been involved in research in melanoma and non-melanoma skin cancer for many years.

Dr. Krekel is a member of the Dutch Workforce on Melanoma (Nederlandse Melanoom Werkgroep) and is a member of the Guideline Committee for Basal

Cell Carcinoma. She is currently the President of the European Society for Micrographic Surgery and a member of the Taskforce for Operative Dermatology of the European Academy for Dermatology and Venereology. She won the European Award in Photodermatology (Athens) in 1996.



Gerard de Haan received the B.Sc., M.Sc., and Ph.D. degrees from Delft University of Technology, Delft, The Netherlands, in 1977, 1979, and 1992, respectively.

He joined Philips Research, Eindhoven, The Netherlands, in 1979. He has led research projects in the area of video processing, and participated in European projects. He has coached students from various universities, and teaches since 1988 for the Philips Centre for Technical Training. Since 2000, he has been a Research Fellow in the Video

Processing and Analysis Group of Philips Research Eindhoven, and a part-time Full Professor at the Eindhoven University of Technology teaching "Video Processing for Multimedia Systems". He has a particular interest in algorithms for motion estimation, video format conversion, and image enhancement. His work in these areas has resulted in a number of books and book chapters, about 135 scientific papers, more than 100 patents and patent applications, and various commercially available ICs.

Dr. de Haan serves in the program committees of various international conferences on image and video processing. He was awarded the 1995, 1997, 1998, 2002, and 2003 ICCE Outstanding Paper Awards. He was the 1998 recipient of the Gilles Holst Award and the 2002 Chester Sall Award from the IEEE Consumer Electronics Society. The Philips "Natural Motion Television" concept, based on his Ph.D. study, received the European Video Innovation Award of the Year 1995 from the European Imaging and Sound Association. In 2001, the successor of this concept "Digital Natural Motion Television" received a Business Innovation Award from the *Wall Street Journal Europe*.